The final version of the article appears in Electrochimica Acta 245 (2017) 1048–1058.
https://doi.org/10.1016/j.electacta.2017.05.052

Physical Modeling of the Proton Density in Nanopores of PEM Fuel Cell Catalyst Layers

Tasleem Muzaffar[1], Thomas Kadyk[1], and Michael Eikerling[1a]

[a] meikerl@sfu.ca

[1]*Department of Chemistry, Simon Fraser University, Burnaby, British Columbia, Canada*

Abstract

In polymer electrolyte fuel cells, a foremost goal is to design catalyst layers with high performance at markedly reduced platinum loading. As a contribution towards this objective, we explore a simplified pore geometry to capture the impact of ionomer structure and metal charging properties on the proton density distribution and conductivity in relevant nanopores. The basic model is a cylindrical tubular pore confined by an ionomer shell and a solid platinum-coated core. The gap region between metal and ionomer is filled with water. We study how the surface charge density at the ionomer and the metal charging relation as well as geometric pore parameters affect the electrochemical performance. The density of charged side chains at the ionomer shell exerts a pronounced impact on the surface charge density at the Pt surface and thereby on the activity of the pore for the oxygen reduction reaction. The key parameter controlling the interplay of surface and bulk charging phenomena is the overlap of the Debye lengths of ionomer and metal surfaces in relation to the width of the gap. It allows distinguishing regions with weak and strong correlation between surface charge densities at ionomer shell and Pt core.

1. Introduction

Polymer electrolyte fuel cells (PEFCs) are touted as energy conversion devices of choice for various transportation systems and backup stationary power supply [1–3]. Their positive attributes include a high theoretical thermodynamic efficiency, high power density, scalability of the total power, and ideal compatibility with hydrogen as a fuel [4–6]. The large-scale commercial deployment of PEFCs hinges on breakthroughs in design and fabrication of innovative materials to increase durability and reduce cost [7,8].

The cathode catalyst layer (CCL) contributes the largest voltage losses in the fuel cell. To minimize these losses, it is paramount to optimize the interplay of oxygen diffusion, proton transport, electron migration, electrochemical surface reactions, and water transport [8]. The CCL consists of three main materials components, viz. carbon (C), platinum (Pt), and ionomer (e.g. Nafion ®) that assemble into a multiphase composite medium [7–11]. An ink solution of these ingredients is either directly sprayed or transferred by a decal method onto the polymer electrolyte membrane to form the electrodes [12]. Nanoparticles of Pt provide the active catalyst surface for the electrochemical reaction. The continuously connected carbon phase provides pathways for electron conduction and the ionomer phase supplies protons. In order for proton transport to happen and render the surface of Pt active for the oxygen reduction reaction (ORR), it is essential that a percolating water phase forms inside of the porous CCL [13]. Water is present in the layer in various phases, as liquid water in pores of carbon and ionomer domains or as interfacial water. Oxygen diffuses through the continuously connected gas pore network before dissolving in water-filled pores and diffusing in the liquid phase towards the catalyst surface.

During the fabrication process, self-organization between component materials leads to the formation of agglomerates with a core region of nanoporous carbon|Pt and a nanoscopic ionomer

skin wrapped around it, as depicted in Fig. 1(a) and (b) [9,14]. This agglomerate structure exhibits a characteristic bimodal porosity [11,13,15,16]. Primary intra-agglomerate pores of 1 to 10 nm size are hydrophilic and are responsible for the proton transport whereas secondary inter-agglomerate pores of 10 to 100 nm size are essential to facilitate the gaseous diffusion of oxygen [16,17]. Water with liquid-like properties in pores is essential to render the Pt surface electrochemically active, as the ORR requires the rapid supply of protons [9,14].

The structure described above presents us with two types of interfaces at the water-filled pore level: one type of interface that forms between water and metallic walls made up of the catalyst and the carbon support and the other type of interface between water and the charged ionomer skin. This allows for two different types of ORR-active pores, one with metallic walls only and one with mixed walls of metal and ionomer, as shown in Fig. 1(c) and (d). The charged interfaces exert a major influence on the proton distribution and hence the reaction rate distribution at the nanopore level. The understanding of the role of these different wall configurations on the proton density distribution in pores is essential for a rational design of highly performing CCLs.

The impact of the surface charge density on the proton concentration in a single water-filled and ionomer-free pore with metallic boundaries was studied by Chan and Eikerling [18]. They developed a model for the ORR in a cylindrical pore with charged metal walls. The model explains the effect of the applied metal potential (active control) on the proton density and electrical potential inside the pore. It demonstrates the importance of charging phenomena at the metal wall for the ORR activity.

In order to assess the performance of the pore, an effectiveness factor, Γ, was employed in Ref. [18]. It is defined as the total current produced by the pore normalized by an "ideal" current, j_{ideal}, that would be obtained if reactant and potential distributions were completely uniform,

$$\Gamma = \frac{\int_0^{\mathrm{L}} j^{\mathrm{v}}(z)\mathrm{d}z}{L j_{\mathrm{ideal}}}, \quad j_{\mathrm{ideal}} = j^{\mathrm{o}} \exp\left(-\frac{\alpha_{\mathrm{c}} \mathrm{F} \eta_{\mathrm{c}}}{\mathrm{R_g} T}\right). \qquad (1)$$

Zenyuk *et al*. [19,20] adopted the effectiveness factor concept proposed by Chan and Eikerling and they employed a similar parameterization of the metal charging relation based on the Stern model. However, in contrast to Chan and Eikerling, Zenyuk *et al*. considered the potential of zero charge (pzc), ϕ_{pzc}, strictly as an experimental parameter and they used a value of $\phi_{\mathrm{pzc}} \cong 0.3\ \mathrm{V_{RHE}}$, obtained for a pristine Pt surface [21–26], as a constant in their study, suggesting that a simple Stern-type metal charging relation could be extrapolated to potentials relevant for the ORR. However, at relevant electrode potentials, $\phi_{\mathrm{M}} > 0.7\ \mathrm{V_{SHE}}$, this approach results in unphysical high positive values of the metal surface charge density, σ_{M}. Based on this oversimplified treatment of metal charging phenomena, Zenyuk *et al*. inferred that alkaline conditions would prevail in the nanopores at potentials relevant for the ORR [19,20].

In contrast, Chan and Eikerling deliberately treated ϕ_{pzc} as a variable parameter to allow for nonlinear and nonmonotonic variations in the metal charging relation, as had been seen in seminal experiment by Frumkin and Petrii [27]. A refined model of the electrified interface that accounts in a self-consistent manner for charging effects caused by oxygen chemisorption at the Pt surface and ordered interfacial water molecules was presented by Huang *et al*. [28,29]. Both treatments, those by Chan and Eikerling [18] and Huang *et al*. [28,29], give acidic conditions in the nanopore under potentials of the ORR.

Chan and Eikerling scaled up their model and validated it against experimental data for ionomer-free ultrathin catalyst layers [18]. Sadeghi *et al.* developed a hierarchical model of a conventional ionomer-impregnated CCL and quantified the performance by expanding the definition of the effectiveness factor [30]. Sadeghi *et al*. found the total effectiveness factor of Pt utilization for a

CCL to be ~ 3 to 4% [30]. This low value of Γ suggests that an improved performance should be achievable through advanced structural design of the CCL, which hinges on the understanding of the impact of charged ionomer and metal walls on the proton density distribution at the pore level.

Nouri-Khorasani *et al*. reported a molecular dynamics study of the proton density distribution in a water-filled nanopore bounded by a slab of Pt oxide and a thin ionomer skin layer. The study revealed a significant impact of chemisorbed oxygen at the Pt surface on the interfacial proton concentration [31].

The objective of the present work is to rationalize the concerted impact of the surface charge densities at ionomer shell and metal phase on the potential and proton density distribution at the nanopore level. The model relates these properties further to the ORR activity of the pore. In the terminology of the nanofluidics literature, the nanopore model is a hybrid of passive control of pore charging by a material with fixed surface charge density, viz. the ionomer film, and active control by a material whose surface charge density is modulated by an applied potential, viz. the metal core [32–40].

Section 2 and 3 introduce and define the model and the input parameters. Section 4 presents an implicit analytical solution to the set of governing equations. Section 5 comprises discussions about effects of side chain density at the ionomer shell, metal|solution interfacial properties, and pore geometry on the electrostatic properties and ORR activity.

2. Model and Methodology

The basic model illustrated in Fig. 2, consists of a coaxial cylindrical configuration. The use of cylindrical coordinates simplifies the problem mathematically and allows for the variation of key geometric parameters, viz. pore width and pore length. In contrast to earlier works on electrostatic

and transport phenomena in nanopores, in which symmetrical charging properties of opposing walls were used [18,29], our geometry considers walls with different and independently controlled charging properties.

The cylindrical core with radius R consists of a solid rod with uniform Pt coating. A cylindrical ionomer shell with radius $R + d$ coaxially surrounds the core. The gap space d, between core and shell is filled with water. The pore opening at $z = 0$ is assumed to form an interface with a proton-conducting polymer electrolyte membrane (PEM), whereas the opposite pore opening at $z = L$ has an interface with a gas diffusion medium through which oxygen is supplied. In radial direction, the water-filled pore has a metal boundary at $r = R$ and an ionomer boundary at $r = R + d$. The charge density at the ionomer wall, σ_{p}, depends on the density of anionic surface groups, a materials property (passive control). The charge density at the metal wall, σ_{M}, is a function of the metal phase potential, $\phi_{\mathrm{M}}^{\mathrm{b}}$ (active control).

To determine the electrochemical performance of the pore, the continuum model developed by Chan and Eikerling [18] and more recently refined by Huang *et al*. [28,29] is adopted, and modified by the inclusion of the fixed σ_{p}. The model relates σ_{p} to σ_{M}, and to the rate of the ORR, using an electric double layer model, transport equations, and a kinetic equation for the interfacial charge transfer. The continuum approach is sufficiently accurate when the pore opening is > 5 times the size of a hydrated proton, which is ~ 3 Å. Continuum models and molecular dynamics studies for proton conduction in water filled cylindrical pores agree well for pore radii > 1 nm, while corrections are required for smaller pores [18–20,30,41–52]. We have restricted our analysis to pore width ≥ 2 nm.

2.1.Governing Equations

It is assumed that protons are only transported by diffusion and migration and the convection term in the Poisson-Nernst-Planck Equation (PNP) is neglected [53,54]. The Nernst-Planck equation,

$$\vec{J}_{\mathrm{H^+}} = -\mathrm{D}_{\mathrm{H^+}}\left(\nabla C_{\mathrm{H^+}} + \frac{\mathrm{F}}{\mathrm{R_g}T} C_{\mathrm{H^+}} \nabla\phi\right), \tag{2}$$

relates the proton flux to the gradients of the solution-phase potential, ϕ, and proton concentration, $C_{\mathrm{H^+}}$, where $D_{\mathrm{H^+}}$ is the diffusion coefficient of protons. Mass conservation of protons is given by the steady state continuity equation,

$$\frac{\partial C_{\mathrm{H^+}}}{\partial t} = -\left(\vec{\nabla}\cdot\vec{J}_{\mathrm{H^+}}\right) = 0. \tag{3}$$

The potential distribution is obtained from the Poisson equation,

$$\nabla^2\phi = -\frac{C_{\mathrm{H^+}}\mathrm{F}}{\epsilon_o\epsilon_r}. \tag{4}$$

The oxygen flux $\vec{J}_{\mathrm{O_2}}$ is given by Fick's law,

$$\vec{J}_{\mathrm{O_2}} = -\mathrm{D}_{\mathrm{O_2}}\left(\nabla C_{\mathrm{O_2}}\right), \tag{5}$$

where $C_{\mathrm{O_2}}$ and $\mathrm{D}_{\mathrm{O_2}}$ are the concentration and diffusivity of oxygen. The Laplace Equation determines the oxygen mass balance,

$$\nabla^2 C_{\mathrm{O_2}} = 0. \tag{6}$$

The reaction plane is assumed to be located at a distance from the metal surface that corresponds to the radius of the hydrated proton. The superscript "‡" indicates a property evaluated at the reaction plane. The faradaic current density at this plane is

$$j^{\ddagger}(\mathrm{z}) = j^{\mathrm{o}} \left(\frac{C^{\ddagger}_{\mathrm{O}_2}(z)}{C^{\mathrm{o}}_{\mathrm{O}_2}}\right)^{\gamma_{\mathrm{O}_2}} \left(\frac{C^{\ddagger}_{\mathrm{H}^+}(z)}{C^{\mathrm{o}}_{\mathrm{H}^+}}\right)^{\gamma_{\mathrm{H}^+}} \exp\left(-\frac{\alpha_{\mathrm{c}}\mathrm{F}\eta^{\ddagger}(z)}{\mathrm{R_g}T}\right), \quad (7)$$

where j^{o} is the exchange current density, γ_{O_2} and γ_{H^+} are reaction orders, $C^{\mathrm{o}}_{\mathrm{O}_2}$ and $C^{\mathrm{o}}_{\mathrm{H}^+}$ denote the reference oxygen concentration at $z = L$ and the reference proton concentration at $z = 0$, respectively, α_{c} is the electronic transfer coefficient and $\eta^{\ddagger}(z)$ is the local overpotential at the reaction plane.

The proton concentration at the reaction interface is given by $C^{\ddagger}_{\mathrm{H}^+}(z)$, and the local overpotential $\eta^{\ddagger}(z)$ at the reaction plane is given by

$$\eta^{\ddagger}(z) = \eta_{\mathrm{c}} - (\phi^{\ddagger}(\mathrm{z}) - \phi^{\mathrm{o}}), \quad (8)$$

where η_{c} is the cathodic overpotential, $\phi^{\ddagger}(\mathrm{z})$ the solution phase potential at the reaction plane, and ϕ^{o} the solution phase potential at $z = 0$.

2.2.Boundary Conditions

The proton concentration at $z = 0$ is $C_{\mathrm{H}^+}(r, 0)$ and the potential at this boundary is ϕ^{o},

$$C_{\mathrm{H}^+}(r, 0) = C^{\mathrm{o}}_{\mathrm{H}^+}, \quad (9)$$

$$\phi(r, 0) = \phi^{\mathrm{o}}. \quad (10)$$

Assuming that the PEM is gas tight, the oxygen flux at $z = 0$ is

$$\vec{J}_{\mathrm{O}_2}(r, 0) \cdot \hat{z} = 0, \quad (11)$$

where $\hat{z}$ is a unit vector in z-direction. At $z = L$, the concentration of dissolved oxygen is obtained using Henry's law,

$$C_{\mathrm{O}_2}(r, L) = \mathrm{H}_{\mathrm{O}_2} p^{\mathrm{o}}_{\mathrm{O}_2}, \quad (12)$$

where H_{O_2} is the Henry's constant and $p^0_{O_2}$ is the partial pressure of oxygen at the interface with the gas diffusion medium. When moving along the pore in axial direction starting from $z = 0$, the proton flux is gradually consumed in the ORR and it goes to zero at $z = L$,

$$\vec{j}_{H^+}(r, L) \cdot \hat{z} = 0. \tag{13}$$

The metal core is considered to be equipotential,

$$\nabla \phi_M(r, L) \cdot \hat{z} = 0. \tag{14}$$

At the reaction interface, both the oxygen and the proton flux are coupled to the reaction current density,

$$\vec{j}^{\ddagger}_{H^+}(z) \cdot \hat{z} = \frac{j^{\ddagger}(z)}{F}, \tag{15}$$

$$\vec{j}^{\ddagger}_{O_2}(z) \cdot \hat{z} = \frac{j^{\ddagger}(z)}{4F}. \tag{16}$$

The charging relation that captures the electrostatic interaction between protons and the charged metal pore walls [28] is given by

$$\begin{aligned} \phi_{OHP} = E_{app} - \Delta\phi_M - \frac{\mu_{PtO}}{\epsilon_{PtO}} + \frac{N_{tot}\mu_w}{\epsilon_{IHP}} \tanh X \\ - \sigma_M \left(\frac{\delta_{PtO}}{\epsilon_{PtO}} + \frac{\delta_{OHP}}{\epsilon_{OHP}} + \frac{\delta_{IHP}}{\epsilon_{IHP}} \right), \end{aligned} \tag{17}$$

where ϕ_{OHP} is the potential at the outer Helmholtz plane, δ_{PtO}, δ_{OHP}, and δ_{IHP} are the thicknesses of the PtO layer, OHP, and IHP respectively; X is the dimensionless total field-dependent adsorption energy of water molecules as defined in [28]; $\Delta\phi_M$ is a constant potential drop at the metal surface due to the electron spillover effect; $\epsilon_{PtO}, \epsilon_{OHP}$, and ϵ_{IHP} are dielectric constants of the PtO layer, OHP, and IHP respectively (in units of the dielectric permittivity of vacuum, ϵ_o);

N_{tot} is the density of adsorption sites at the metal surface, which we replace by the Pt surface atom density, and μ_w is the dipole moment of water. An expression for ϕ_{OHP} will be presented in Eq.34 obtained for the specific model geometry considered in this article. The surface oxide dipole density μ_{PtO} is calculated from Eq. 5, 7-8 in Ref. [28].

$$\mu_{\mathrm{PtO}} = N_{\mathrm{tot}}\mu_{\mathrm{site}}, \tag{18}$$

with μ_{site} being the average dipole moment per surface Pt atom,

$$\mu_{\mathrm{site}} = \theta_{\mathrm{Ox}}(\varsigma e)\delta_{\mathrm{PtO}}, \tag{19}$$

where ς is the fractional charge number assigned to surface metal atoms and oxygen atoms in the oxide dipole layer. In Eq. 19, θ_{Ox} is the normalized oxide coverage, given by

$$\frac{\mathrm{F}\left(\phi_{\mathrm{M}}^{\mathrm{b}} - \phi^{\mathrm{s}} - E_{\mathrm{Ox}}^{\mathrm{o}}\right)}{\mathrm{R_g T}} + (2.3)pH^{\mathrm{s}} = \ln\left(\frac{\theta_{\mathrm{Ox}}}{1-\theta_{\mathrm{Ox}}}\right) + \frac{\psi_{\mathrm{Ox}}\theta_{\mathrm{Ox}}}{\mathrm{R_g}T}, \tag{20}$$

where pH^{s} represents the pH on the surface of the metal and can be transformed into $\phi^{\ddagger}$ using the Boltzmann relation; ψ_{Ox} is the lateral interaction parameter of chemisorbed oxygen species, $\phi_{\mathrm{M}}^{\mathrm{b}}$ is the bulk metal potential, ϕ^{s} is the interfacial potential in the water phase, and $E_{\mathrm{Ox}}^{\mathrm{o}}$ represents the equilibrium potential of oxide layer formation as explained in Ref. [28];

The free metal surface charge density σ_{M} is related to the gradient of potential via Gauss law,

$$\sigma_{\mathrm{M}} = \epsilon_s \left.\frac{\mathrm{d}\phi(r)}{\mathrm{d}r}\right|_{\mathrm{OHP,\ z}}. \tag{21}$$

where ϵ_s is the dielectric constant of the solvent in the gap region (in units of ϵ_o) .

The boundary condition at the charged ionomer wall is

$$\sigma_{\mathrm{p}} = \epsilon_s \left.\frac{\mathrm{d}\phi(r)}{\mathrm{d}r}\right|_{R+d,\ \mathrm{z}} . \qquad (22)$$

For simplicity, the anionic charges at the ionomer skin layer are assumed to be located directly at the wall. The ionomer interface is assumed to be impermeable to oxygen. This assumption defines a worst-case scenario, as all oxygen must transport through the water filled pore volume, a pathway that always exists. This assumption allows for a simplified axial boundary condition for oxygen presented in section 4.

3. Model Parameters

The values of model parameters are listed in the Table 1. For the geometry, we assume that R is in the range of the size of a typical Pt nanoparticle, i.e., $2-4$ nm. As discussed below, the main geometric parameter of the model is the gap width, d. Normally, d is expected to be < 2 nm. For $d \sim R$ the curvature in the cylindrical geometry will exert a strong impact on the model solution. For $d \ll R$, the solution will approach the limiting case of a flat slab-like pore.

The typical range of variation of L is from 50 nm to 100 nm. For practical considerations, L could correspond to the pore length encountered in flooded agglomerates of conventional CCLs, which are gas-diffusion electrodes, *cf.* Fig. 1, or to the pore length in electrolyte-flooded ultrathin CCLs. The potential decay region at the pore interface with the PEM, corresponding to the Donnan potential difference, extends over a width of about 4 Å that is very small compared to L; this region thus has a negligible impact on the electrostatic properties of the pore.

As we will explain in section 4, the proton density and solution phase potential assume quasi-equilibrium distributions in the model, which are insensitive to L. The distribution of the oxygen concentration and ORR activity along the pore are highly sensitive to L, when L exceeds the

oxygen penetration depth δ [8,18]. In flooded pores, δ lies typically in the range of ~ 100 nm; it could be reduced if the pore surface is highly ORR active.

The nearest neighbor separation distance l_{c} of sidechains lies in the range of 0.7 to 1.2 nm [9]. Considering a side chain arrangement in a square lattice, the relation between l_{c} and σ_{p} is given by

$$\sigma_{\mathrm{p}} = -\frac{e_o}{{l_{\mathrm{c}}}^2}, \qquad (23)$$

where e_o is the elementary charge. For a hexagonal arrangement of surface groups at the ionomer film, the relation is

$$\sigma_{\mathrm{p}} = -\frac{2e_o}{\sqrt{3}{l_c}^2}. \qquad (24)$$

The metal surface charge density depends on the value of the metal potential relative to the potential of zero charge (pzc). The pzc is a measure of the propensity of a metal to retain negative charge at the surface. However, the recent work by Huang *et al*. [28,29] has shown that ϕ_{pzc} is not sufficient as a descriptor of metal charging phenomena.. In the presence of chemisorbed species at the metal surface, Frumkin and Petrii [27] and Trasatti [55] introduced the notions of the potential of zero free charge and the potential of zero total charge.

Another peculiar observation by Frumkin and Petrii was the “inverse” potential of zero free charge [27]. As the potential increases, the surface charge climbs to more positive values, as expected. However, in the potential region of oxygen chemisorption, the charge density decreases with increasing potential, goes through an “inverse” potential of zero charge and then assumes negative charge density values again [27,56].

The model of Huang *et al.* [28,29] reproduces this non-monotonic behavior. In the hydrogen adsorption region and the double layer charging region, that is for $\phi_{\mathrm{M}}^{\mathrm{b}} < 0.6\ \mathrm{V}_{SHE}$, σ_{M} increases with $\phi_{\mathrm{M}}^{\mathrm{b}}$. In the potential region of oxygen chemisorption, the relation between σ_{M} and $\phi_{\mathrm{M}}^{\mathrm{b}}$ goes through a maximum and then it exhibits a downward turn. σ_{M} is negative at high potentials, that is for $\phi_{\mathrm{M}}^{\mathrm{b}} > 0.8\ \mathrm{V}_{SHE}$, as seen in the Fig. 6 of Ref. [28]. The negative charging region at high potential was also observed as well by Garcia-Araez et al.[57]. In our work, the formalism of Huang et al. [28,29] is adopted, as described in Section 2.2.

For the kinetic parameters of the ORR, we use $\alpha_{\mathrm{c}} = 1$ and $\gamma_{\mathrm{H^+}} = 1.5$ in the high potential region, and $\alpha_{\mathrm{c}} = 0.5$, $\gamma_{\mathrm{H^+}} = 1.0$ in the low potential region [58–60], following the rationale presented in Chan and Eikerling [18]. The transition between the two potential regions occurs at $\eta_{\mathrm{c}} = -0.4\ V$ [61–65].

4. Model Solution

Because of the slow ORR kinetics, the PNP Equation is reduced to the Poisson-Boltzmann (PB) equation. The PB equation is solved analytically and the solution is analyzed for the considered ranges of radii, length and potential. This approximation allows solving for potential and reactant concentration profiles analytically and factorizing Γ into separate factors due to electrostatic and oxygen transport effects.

4.1.Electrostatic Problem

Setting the flux term on the left-hand side of Eq. 2 equal to zero gives an equation in the form of the PB equation in cylindrical co-ordinates,

$$\frac{1}{r}\left(\frac{\partial}{\partial r}\right)\left(r\frac{\partial}{\partial r}\right)\phi + \frac{\partial^2}{\partial z^2}\phi = -\frac{C_{\mathrm{H^+}}^{\mathrm{o}}\mathrm{F}}{\epsilon_{\mathrm{s}}}\exp[-b(\phi(R,z)-\phi^{\mathrm{o}})] \quad \text{with } \mathrm{b} = \frac{\mathrm{F}}{\mathrm{R_g}T}. \tag{25}$$

To simplify notations, equations are non-dimensionalized by using the substitutions

$$\nu = \frac{r}{R}, r = \nu R, dr = Rd\nu,$$

$$\xi = \frac{z}{L}, \; z = \xi L, \; dz = Ld\xi, \text{ and } \Phi = \frac{\mathrm{F}\phi}{\mathrm{R_g}T}.$$

We thus obtain

$$\Phi\frac{1}{\nu}\left(\frac{\partial}{\partial\nu}\right)\left(\nu\frac{\partial\Phi}{\partial\nu}\right) + \frac{R^2}{L^2}\frac{\partial^2\Phi}{\partial\xi^2} = -\frac{\mathrm{R}^2}{{\lambda_{\mathrm{D}}}^2}\exp\left(-(\Phi(\nu)-\Phi^{o})\right) \tag{26}$$

where $\lambda_{\mathrm{D}} = \sqrt{\frac{\epsilon_{\mathrm{s}}\mathrm{R_g}T}{C_{\mathrm{H^+}}^{\mathrm{o}}\mathrm{F}^2}}$ is the Debye length. The dimensionless boundary conditions are

$$\left.\frac{\mathrm{d}\Phi(\nu)}{\mathrm{d}\nu}\right|_{\nu=1+\frac{d}{R}} = -\frac{\sigma_{\mathrm{p}}\mathrm{F}}{\epsilon_{\mathrm{s}}\mathrm{R_g}T}R, \text{and} \tag{27}$$

$$\left.\frac{\mathrm{d}\Phi(\nu)}{\mathrm{d}\nu}\right|_{\nu=1} = -\frac{\sigma_{\mathrm{M}}\mathrm{F}}{\epsilon_{\mathrm{s}}\mathrm{R_g}T}\,R. \tag{28}$$

The following simplifications convert the 2D model into a 1D +1D model. For high aspect ratios, i.e. $L \gg d$, the second term on the left-hand side of Eq. 26 becomes negligibly small, as verified by comparison with the exact numerical solution. Due to the high electronic conductivity, the potential decay region at the $z = 0$ boundary is limited to a small region with thickness of the order of the Debye length, $\lambda_{\mathrm{D}} \sim 0.4$ nm. Ignoring the contribution of this region for the overall rate of current generation in the pore, one can set $\frac{\partial^2\Phi}{\partial\xi^2} = 0$, which reduces the electrostatic problem to a radial problem. This means that the proton concentration varies only in radial direction, $C_{\mathrm{H^+}} =$

$C_{H^+}(r)$. A comparison of the approximate model solution obtained with this 1D approach with the full numerical solution of Eq. 26 confirms that the 1D approximation is sufficiently accurate.

As can be seen in the Fig. 1(a) and (b), in a partially ionomer covered agglomerate, oxygen molecules for the ORR reach the Pt surface by diffusion through the ionomer thin film as well as by diffusion through the water filled pores, defining a complex mixed-phase or random network-type diffusion problem. The solution of this transport problem is beyond the scope of this article and we have made the simplifying assumption that the ionomer shell blocks oxygen diffusion, implying that oxygen transport must take place by dissolving oxygen in liquid water, as stated earlier. It is self-evident that the liquid-water based diffusion mechanism is crucial; without it the major fraction of the Pt surface area, embedded inside of water-filled agglomerate pores, would be inactive. Recent efforts in modeling transport and reaction in individual nanopores or ionomer free catalyst layers [18,29] lend credibility to this view.

Moreover, the diffusion of dissolved oxygen through water in agglomerates was considered in a hierarchical model of catalyst layer operation that reproduced very well experimental voltage vs. current density curves [30].

We are aware of a common conjecture that diffusion of oxygen through the ionomer skin surrounding C|Pt particles or agglomerates is a performance-limiting process [70,71]. However, as will be seen from results of pore level modeling presented below, oxygen diffusion through the ionomer skin is not essential for the ORR activity of a typical nanopore under normal conditions and it will not become performance-limiting under critical conditions, when CCL flooding occurs, justifying neglect of this contribution.

For high aspect ratio, i.e. $L \gg d$ considered throughout this work, oxygen concentration varies only along the axial direction and it is uniform in the radial direction $\left(\frac{\partial C_{O_2}}{\partial r} = 0\right)$. These simplifications reduce the 2D model to a 1D model for proton density and potential profile in radial direction and a 1D model for oxygen concentration in axial direction. The model equation for the potential reduces to

$$\frac{1}{\nu}\left(\frac{\partial}{\partial \nu}\right)\left(\nu \frac{\partial \Phi}{\partial \nu}\right) = -\frac{R^2}{{\lambda_{\mathrm{D}}}^2}\exp\left(-(\Phi(\nu) - \Phi^o)\right). \tag{29}$$

The solution of Eq. 29 is

$$\Phi(\nu) - \Phi^{\mathrm{o}} = \ln\left(\frac{\Lambda^2 \nu^2 \sinh\left(\frac{\chi(\ln(\nu) + c_2)}{2}\right)^2}{\chi^2}\right), \tag{30}$$

where χ and c_2 are integration constants. Using boundary conditions Eq. 27 and 28 in Eq. 30 gives

$$\begin{aligned}\left.\frac{\mathrm{d}\Phi(\nu)}{\mathrm{d}\nu}\right|_{\nu=1+\frac{d}{R}} &= -\frac{\sigma_{\mathrm{p}}\mathrm{F}}{\mathrm{R_g}T}R \\ &= \frac{2R}{R+d}\left(1 + \chi\coth\left(\frac{\chi\left(\ln\left(\frac{R+d}{R}\right) + c_2\right)}{2}\right)\right),\end{aligned} \tag{31}$$

$$\left.\frac{\mathrm{d}\Phi(\nu)}{\mathrm{d}\nu}\right|_{\nu=1} = -\frac{\sigma_{\mathrm{M}}\mathrm{F}}{\mathrm{R_g}T}\,R = \left(2 + 2\chi\coth\left(\frac{\chi c_2}{2}\right)\right), \tag{32}$$

$$\left(\frac{0.6}{\pi\delta_{\mathrm{IHP}}^2} + N_{\mathrm{tot}}\right)\left(\frac{N_A\mu_{\mathrm{w}}^2}{\mathrm{R_g}T\delta_{\mathrm{IHP}}\epsilon_{\mathrm{IHP}}}\right)\tanh X - X = \frac{N_A\mu_{\mathrm{w}}\sigma_{\mathrm{M}}}{\epsilon_{\mathrm{IHP}}\mathrm{R_g}T}, \tag{33}$$

$$\ln\left(\frac{\Lambda^2 \sinh\left(\frac{\chi c_2}{2}\right)^2}{\chi^2}\right)$$

$$= E_{\text{app}} - \Delta\Phi_{\text{M}} - \frac{\mu_{\text{PtO}}}{\epsilon_{\text{PtO}}} + \frac{N_{\text{tot}}\mu_w}{\epsilon_{\text{IHP}}}\tanh X \qquad (34)$$

$$- \sigma_{\text{M}}\left(\frac{\delta_{\text{PtO}}}{\epsilon_{\text{PtO}}} + \frac{\delta_{\text{OHP}}}{\epsilon_{\text{OHP}}} + \frac{\delta_{\text{IHP}}}{\epsilon_{\text{IHP}}}\right),$$

where N_A is the Avogadro's number. Equation (31) to (34) must be solved together with Eq. 20 to find the parameters χ, c_2, σ_{M}, θ_{Ox}, and X.

The effectiveness factor of Pt utilization for the ORR is given by

$$\Gamma = \int_0^L \left(C_{\text{O}_2}^{\ddagger}\right)^{\gamma_{\text{O}_2}} \exp\left((\alpha_{\text{c}} - \gamma_{\text{H}^+})(\Phi^{\ddagger} - \Phi^{\text{o}})\right) dz. \qquad (35)$$

Since $\Phi^{\ddagger}$ is independent of z, Γ decouples into factors representing electrostatic and oxygen transport effects,

$$\Gamma = \Gamma_{\text{elec}}\Gamma_{\text{O}_2}, \qquad (36)$$

with

$$\Gamma_{\text{elec}} = \exp\left((\alpha_{\text{c}} - \gamma_{\text{H}^+})(\Phi^{\ddagger} - \Phi^{\text{o}})\right), \qquad (37)$$

$$\Gamma_{\text{O}_2} = \int_0^L \left(C_{\text{O}_2}^{\ddagger}\right)^{\gamma_{\text{O}_2}} dz. \qquad (38)$$

By using Eqs. 17, 30, and 37 at the OHP, we obtain

$$\frac{\ln(\Gamma_{\text{elec}})}{\alpha_{\text{c}}-\gamma_{\text{H}^+}} = E_{\text{app}} - \Delta\Phi_M - \frac{\mu_{\text{PtO}}}{\epsilon_{\text{PtO}}} + \frac{N_{\text{tot}}\mu_w}{\epsilon_{\text{IHP}}}\tanh X - \left(2 - \sqrt{\chi^2 + \Lambda^2\Gamma_{\text{elec}}{}^{\left(\frac{1}{\gamma_{\text{H}^+}-\alpha_{\text{c}}}\right)}}\right)\left(\frac{\delta_{\text{PtO}}}{\epsilon_{\text{PtO}}} + \frac{\delta_{\text{OHP}}}{\epsilon_{\text{OHP}}} + \frac{\delta_{\text{IHP}}}{\epsilon_{\text{IHP}}}\right). \quad (39)$$

Eq. 39 is solved numerically at different values of σ_{p}.

To analyze the charging behavior of the pore, we calculated the differential capacitance as a function of σ_{p} and $\Phi_{\text{M}}^{\text{b}}$. The total accumulated proton charge in the pore is

$$Q = 2\pi L\left(\sigma_{\text{p}}(R+d) + \sigma_{\text{M}}R\right). \quad (40)$$

Since σ_{p} is fixed, the differential pore capacitance C_{diff} is obtained from

$$C_{\text{diff}} = \frac{\partial\sigma_{\text{M}}}{\partial V}, \qquad \partial V = \partial\Phi_{\text{M}}^{\text{b}}. \quad (41)$$

4.2.Oxygen Transport

The 1D oxygen diffusion equation is

$$\frac{\text{d}^2C_{O_2}(z)}{\text{d}z^2} - \gamma_{\text{R}}{}^2C_{O_2} = 0. \quad (42)$$

$$\gamma_{\text{R}}{}^2 = \lambda_{\text{R}}{}^{-2} = \frac{k^{\text{o}}}{\text{D}_{\text{O}_2}L}\left(\frac{C_{\text{H}^+}^{\ddagger}}{C_{\text{H}^+}^{\text{o}}}\right)^{\gamma_{\text{H}^+}}\exp\left(\frac{-\alpha_{\text{c}}\text{F}\eta_{\text{c}}}{\text{R}_{\text{g}}T}\right), \quad (43)$$

where λ_{R} is the reaction penetration depth and k^{o} is the ORR rate constant. With the boundary conditions,

$$\frac{\mathrm{d}C_{O_2}(z=0)}{\mathrm{d}z} = 0 \text{ and } C_{O_2}(z=L) = C_{O_2}^{o} \tag{44}$$

Eq. 44 has the analytical solution

$$C_{\mathrm{O_2}}(\mathrm{z}) = C_{\mathrm{O_2}}^{\mathrm{o}} \frac{\cosh(\gamma_{\mathrm{R}} z)}{\cosh(\gamma_{\mathrm{R}} L)}. \tag{45}$$

5. Results and Discussion

5.1.Electrostatic Problem

First, we analyze the influence of $\sigma_{\mathrm{p}}$and $\phi_{\mathrm{M}}^{\mathrm{b}}$ on $C_{\mathrm{H^+}}$ and the electrostatic potential profile across the pore. Fig. 3(a) and (b) show that protons accumulate at both interfaces. The variation of $\phi_{\mathrm{M}}^{\mathrm{b}}$ in Fig. 3(a) has a slight impact on the proton density and potential, both at the metal interface and the ionomer interface. It is evident from Fig. 3(b), that the side chain density of the ionomer film largely affects the potential and proton density at both interfaces.

For further discussion of charging effects, we introduce a total Debye length, λ_{Dt}, defined as the sum of the Debye lengths at the metal interface, λ_{DM} , and at the ionomer interface, λ_{Dp},

$$\lambda_{\mathrm{Dt}} = \lambda_{\mathrm{DM}} + \lambda_{\mathrm{Dp}} \tag{46}$$

with

$$\lambda_{\mathrm{DM}} = \sqrt{\frac{\epsilon_{\mathrm{s}} \mathrm{R_g} T}{C_{\mathrm{H^+}}^{\mathrm{OHP}} \mathrm{F}^2}}, \qquad \lambda_{\mathrm{Dp}} = \sqrt{\frac{\epsilon_{\mathrm{s}} \mathrm{R_g} T}{C_{\mathrm{H^+}}^{R+d} \mathrm{F}^2}}, \tag{47}$$

where $C_{\mathrm{H^+}}^{\mathrm{OHP}}$ and $C_{\mathrm{H^+}}^{R+d}$ are the proton concentration at OHP and $R + d$ respectively. The parameter λ_{Dt} helps defining a characteristic value of σ_{p} at which the ionomer starts to affect $C_{H^+}^{\ddagger}$. For $\lambda_{\mathrm{Dt}} < d$, the values of $C_{\mathrm{H^+}}$ close to the two interfaces are controlled independently by the

respective surface charge densities. For $\lambda_{\mathrm{Dt}} > d$, the double layers overlap and σ_{p} exerts a strong impact on $C_{H^+}^{\ddagger}$at the metal interface – this will be the normal situation encountered in CCLs.

Fig. 4(a) shows that more negative σ_{p} incurs a shift of σ_{M} to more negative values. This shift in σ_{M} is controlled by the double layer overlap. At large negative values of σ_{p} and small pore width, we expect highly negative σ_{M}. In this figure, we can see two opposing effects: on the one hand, ionomer induces a negative charge on the metal surface; on the other hand, based on the Pt oxide equation used by Huang *et al*. [28,29], at low pH, a poor oxide coverage and resulting smaller oxide dipole moment would render the metal positively charged at intermediate potentials in ionomer free pores. In the system with ionomer, the effect of the ionomer-induced negative charge is dominant. For comparison, σ_{M} for the situation with $\sigma_{\mathrm{p}} = 0$ resembling an ionomer free pore is shown in Fig. 4(b). In this case, $\phi_{\mathrm{M}}^{\mathrm{b}}$ controls $C_{\mathrm{H^+}}$ inside the pore, as has been shown by Chan and Eikerling [18].

At high potentials, a concerted effect of chemisorbed oxygen and ionomer on σ_{M} is discernible. At sufficiently large absolute values of σ_{p} (e.g. $|\sigma_{\mathrm{p}}| = 0.65\ \mathrm{Cm^{-2}}$), σ_{M} is an order of magnitude more negative than the surface charge density in an ionomer free system. The ionomer acts as a proton reservoir and controls the $C_{\mathrm{H^+}}$ distribution inside the pore. This ionomer-induced enhancement effect vanishes for as $|\sigma_{\mathrm{p}}| \rightarrow 0$, as can be seen in Fig. 4(a).

To refine the discussion of the ionomer-effect on metal surface charging, we can distinguish two distinct charging regions in Fig. 4(c), which both exhibit roughly linear correlations between, σ_{p} and σ_{M}. For the given set of basic pore properties defined in Table 1, the characteristic value of $|\sigma_{\mathrm{p}}|$ for the transition between these regions is $|\sigma_{\mathrm{p}}| = 0.15\ \mathrm{Cm^{-2}}$. For $|\sigma_{\mathrm{p}}| > 0.15\ \mathrm{Cm^{-2}}$, the approximate correlation between metal and ionomer surface charge density is $\sigma_{\mathrm{M}} \sim 0.2\,\sigma_{\mathrm{p}}$. For

$|\sigma_p| < 0.15\ \mathrm{Cm^{-2}}$, the correlation is $\sigma_M \sim 0.5\,\sigma_p$. The transition between the two regions is governed by λ_{Dt}. We see a strong impact of σ_p on σ_M, when $\lambda_{Dt} > d$, and a weak impact when $\lambda_{Dt} < d$.

Fig. 5 shows the effect of the ϕ_M^b and σ_p on Γ_{elec}. We see similar behavior as in Fig.4(a): the value of Γ_{elec} increases as $|\sigma_p|$ grows. $\Gamma_{elec}(\phi_M^b)$ goes through a minimum at $\phi_M^b \sim 0.78$ V before assuming higher values at higher potentials due to the concerted effect of chemisorbed oxygen and ionomer. As can be seen from Fig. 5(a), Γ_{elec} assumes values > 1 for large values of $|\sigma_p| > 0.15\ \mathrm{Cm^{-2}}$ due to the increased C_{H^+}. At low potentials $\phi_M^b < 0.6\ V_{SHE}$, this overcharging of the pore is a result of the negative charge on the metal that is induced by the ionomer. At higher potentials $\Phi_M^b > 0.7\ V_{SHE}$, the overcharging results from the concerted effect of both the ionomer induced negative charge and the chemisorbed oxygen. Fig. 5(c) shows that Γ_{elec} assumes high values (> 1) for $|\sigma_p| > 0.15\ \mathrm{Cm^{-2}}$.

For $|\sigma_p| < 0.15\ \mathrm{Cm^{-2}}$, Γ_{elec} is strongly correlated with σ_p indicating a drastic decline in the electrostatic performance of the pore as $\sigma_p \to 0$. This transition between the two charging regimes is controlled by the double layer overlap effect. For comparison, Γ_{elec} is shown as a function of ϕ_M^b for the case $\sigma_p = 0$ in Fig. 5(b).

In the double layer overlap region, electrostatic and transport phenomena in the pore are controlled by the surface charging effects [33,72]; our study shows that in this regime, σ_p exerts a strong impact on σ_M and thus on the performance of the pore as an electrocatalytic medium for the ORR.

Fig. 6 shows the effect of σ_p on C_{diff}. More negative σ_p results in higher C_{H^+} across the pore and more negative σ_M. This leads to an increase of C_{diff}, similar to the trend observed in Γ_{elec} (Fig.

5(c)). This increase in C_{diff} is due to the induced charge by the ionomer and is amplified at high potentials by the additional effect of the chemisorbed oxygen.

We also studied the impact of the pore geometry on σ_{M} and Γ_{elec}. The impact of R and d in Fig. 7(a) shows that a closer proximity of the ionomer interface to the metal interface results in more negative σ_{M} due to the increased $C_{\mathrm{H^+}}$ caused by enhanced double layer overlap under pore confinement. The effect of pore confinement on Γ_{elec} is illustrated in Fig. 7(b). As can be seen in Fig. 7(a) and (b), as the width of the gap region increases, the absolute value of σ_{M} decreases, causing the decline of Γ_{elec}, reflecting the waning impact of the ionomer skin.

We analyzed the radial curvature effect on the pore behavior by varying the ratio $\frac{d}{R}$ at fixed value of d. As can be seen in Fig. 7(c), when $\frac{d}{R}$ decreases from $\frac{d}{R} = 1$, representing a strong curvature to the limit of a flat slab-like pore i.e., $\frac{d}{R} \to 0$, the metal surface charge decreases by ~ 25%.

As we can see from Figs. 4-7, the impact of σ_{p} on σ_{M} and Γ_{elec} is highly nonlinear. Two regions can be distinguished: (1) for small $|\sigma_{\mathrm{p}}| < 0.15\ \mathrm{Cm^{-2}}$, σ_{M} and Γ_{elec} are strongly dependent on σ_{p}; for large $|\sigma_{\mathrm{p}}| > 0.15\ \mathrm{Cm^{-2}}$, σ_{M} and Γ_{elec} exhibit a weak dependence on σ_{p}. The characteristic value of σ_{p} that is seen to control transition between the two regions is mildly dependent upon other model parameters. Overall, Γ_{elec} is significantly enhanced in a partially ionomer-bound pore as compared to an ionomer-free ("all-metallic") pore due to the impact of σ_{p} on the proton density.

5.2.Oxygen Transport Limitation Problem

The profiles for $C_{\mathrm{O_2}}$ are plotted in Figs. 8(a) and (b) for varying η_{c} and L. At $\eta_{\mathrm{c}} < -0.45$ V, O_2 is depleted along the pore as can be seen in Fig. 8(a). For this range of overpotentials, the active part

of the pore is pinned to a thin slab close to $z = L$. Fig. 8(b) illustrates the effect of the length of the pore on the C_{O_2} profile. For $\lambda_R > L$, C_{O_2} is uniformly distributed and independent of pore length.

The effect of the oxygen transport limitations on Γ is captured in the expression

$$\Gamma_{O_2}(z) = \frac{1}{\gamma_R L}\tanh(\gamma_R L). \qquad (48)$$

For $\lambda_R > L$, in Eq. 48 $\tanh(\gamma_R L) \approx \gamma_R L$ and

$$\Gamma_{O_2}(z) \approx 1. \qquad (49)$$

In this limit, Γ is solely determined by Γ_{elec}, as can be seen in Fig. 9(a). In the limit $L > \lambda_R$, we find

$$\Gamma_{O_2}(z) \approx \frac{1}{L\gamma_R}, \quad \text{and } \Gamma \approx \Gamma_{elec}\frac{1}{L\gamma_R}. \qquad (50)$$

In this limit, the impact of oxygen transport on Γ is shown in Fig. 9(a), with Γ_{elec} plotted as a dotted line for comparison. The interplay of increasing C_{H^+} resulting from σ_p and depleting C_{O_2} leads to a maximum in the plot of Γ vs η_c in Figs. 9(a) and (b). With increasing L, the maximum in Γ shifts towards more positive overpotentials as the O_2 transport limitation becomes more severe. Fig. 9(b) compares a pore with charged ionomer shell to one with an uncharged shell ($\sigma_p = 0$). The pore with charged ionomer wall exhibits an enhancement of the effectiveness factor of Pt utilization by about a factor 8. It is evident that σ_p markedly impacts pore performance and this effect should be considered in efforts to improve catalyst layer design.

6. Conclusion

We have presented a pore-scale model with mixed boundaries made of a charged metal core and an ionomer skin layer. The study rationalizes the impact of the charging properties of both boundaries on the potential and proton density distributions in the water-filled gap confined by these surfaces and it correlates these properties to the ORR performance of the pore. The most crucial parameter controlling the pore performance is the ionomer surface charge density. We found a significantly enhanced pore performance for values of the ionomer surface charge density and pore geometries for which the total Debye length is greater than the pore width. At lower applied potential, we found a strong impact of the ionomer surface charge density on the metal surface charge density and the effectiveness factor for the ORR. At higher potentials, the combined effects of ionomer surface charge density and chemisorbed oxygen, weaken the net impact on the metal surface charge density. The performance enhancement exerted by the charged ionomer skin is seen by comparison with a non-charged case. The effectiveness factor for the ORR is enhanced by a factor of ~ 8 for a system with highly charged ionomer skin. The effect of the pore geometry on performance was also explored. Pores with smaller width of the water-filled gap show enhanced performance due to the pore confinement effect. All in all, findings presented in this article reveal the important concerted impact of the density of charged sidechain at the ionomer skin and of the surface charging relation of the metal on the pore performance. Both of these structure-related properties should be considered in efforts to design and fabricate advanced catalyst layers.

Acknowledgements

The authors gratefully acknowledge financial assistance by an Automotive Partnership Canada grant, file number APCPJ417858, that supports the Catalysis Research for Polymer Electrolyte Fuel Cells(CaRPE-FC) network.

Figure Captions

Figure 1. (a) Schematic of catalyst layer structure with agglomerates (b) Schematic of single agglomerate structure with primary pores. (c) Pore with all metallic walls. (d) Pore with mixed boundaries of charged metal wall and charged ionomer skin wall.

Figure 2. Schematic of a single pore with both mixed ionomer and metal walls. The pore interfaces at one opening with a proton supplying medium and at the other end with an oxygen diffusion medium.

Figure 3. Radial profile of $C_{\mathrm{H^+}}$ from metal interface to the ionomer interface (a) at different values of $\phi_{\mathrm{M}}^{\mathrm{b}}$ and fixed value of $\sigma_{\mathrm{p}} = -0.65\ \mathrm{Cm^{-2}}$. (b) at different σ_{p} and fixed $\phi_{\mathrm{M}}^{\mathrm{b}} = 0.7\ \mathrm{V}_{SHE}$. ($d = 4\ \mathrm{nm}, L = 100\ \mathrm{nm}$).

Figure 4. (a) σ_{M} as a function of $\phi_{\mathrm{M}}^{\mathrm{b}}$ for different values of σ_{p}. (b) σ_{M} as a function of $\phi_{\mathrm{M}}^{\mathrm{b}}$ for $\sigma_{\mathrm{p}} = 0\ \mathrm{Cm^{-2}}$. (c) σ_{M} as a function of σ_{p}. ($d = 4\ \mathrm{nm},\ L = 100\ \mathrm{nm}$)

Figure 5. (a) Γ_{elec} as a function $\phi_{\mathrm{M}}^{\mathrm{b}}$ of for different values σ_{p}. (b) Γ_{elec} as a function of $\phi_{\mathrm{M}}^{\mathrm{b}}$ for $\sigma_{\mathrm{p}} = 0\ \mathrm{Cm^{-2}}$. (c) Γ_{elec} as a function of σ_{p}. ($d = 4\ \mathrm{nm},\ L = 100\ \mathrm{nm}$)

Figure 6. The differential pore capacitance, C_{diff}, as a function of σ_{p} ($d = 4\ \mathrm{nm},\ L = 100\ \mathrm{nm}$).

Figure 7. (a) σ_{M} as a function of $\phi_{\mathrm{M}}^{\mathrm{b}}$ for varying pore width. ($L = 100\ \mathrm{nm}$). (b) Γ_{elec} as a function of $\phi_{\mathrm{M}}^{\mathrm{b}}$ for varying pore width ($L = 100\ \mathrm{nm}$) (c) σ_{M} as a function of $\phi_{\mathrm{M}}^{\mathrm{b}}$ for varying R at constant d (approaching the limit of flat slab like pore); ($d = 4\ \mathrm{nm}, L = 1\ \mu\mathrm{m}$)

Figure 8. (a) C_{O_2} profile across the pore at different η_c ($d = 4$ nm, $L = 20$ nm) (b) C_{O_2} profile across the pore as a function of L for $\eta_c = -0.30$ V. ($d = 4$ nm).

Figure 9. (a) Γ as a function of η_c at different L ($d = 4$ nm) (b) Γ as a function of η_c at different σ_P ($d = 4$ nm)

Table Captions

Table 1. Parameters used in the model

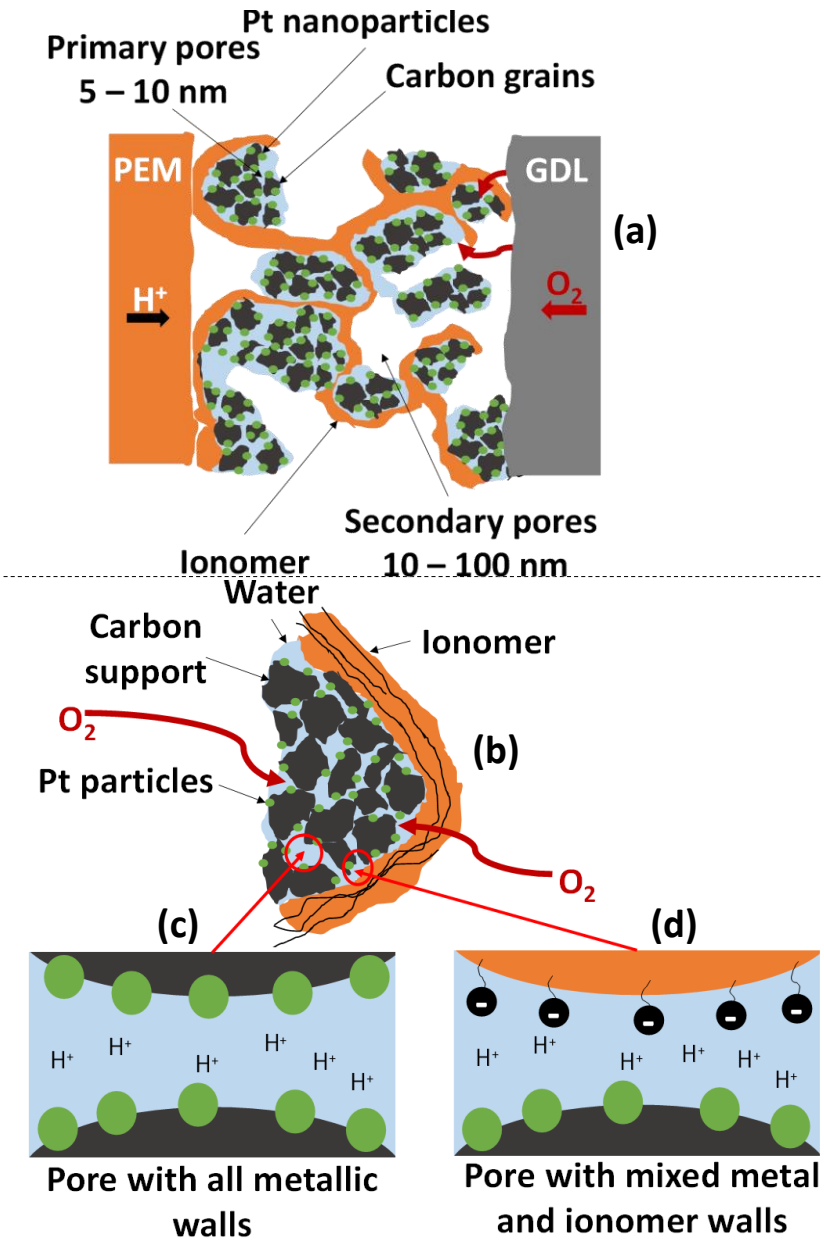
Pt nanoparticles
Primary pores
5 – 10 nm
Carbon grains
PEM
GDL
(a)
H+
O2
Secondary pores
10 – 100 nm
Ionomer
Water
Carbon
support
Ionomer
O2
(b)
Pt particles
O2
(c)
(d)
H+
Pore with all metallic
walls
Pore with mixed metal
and ionomer walls

Figure 1

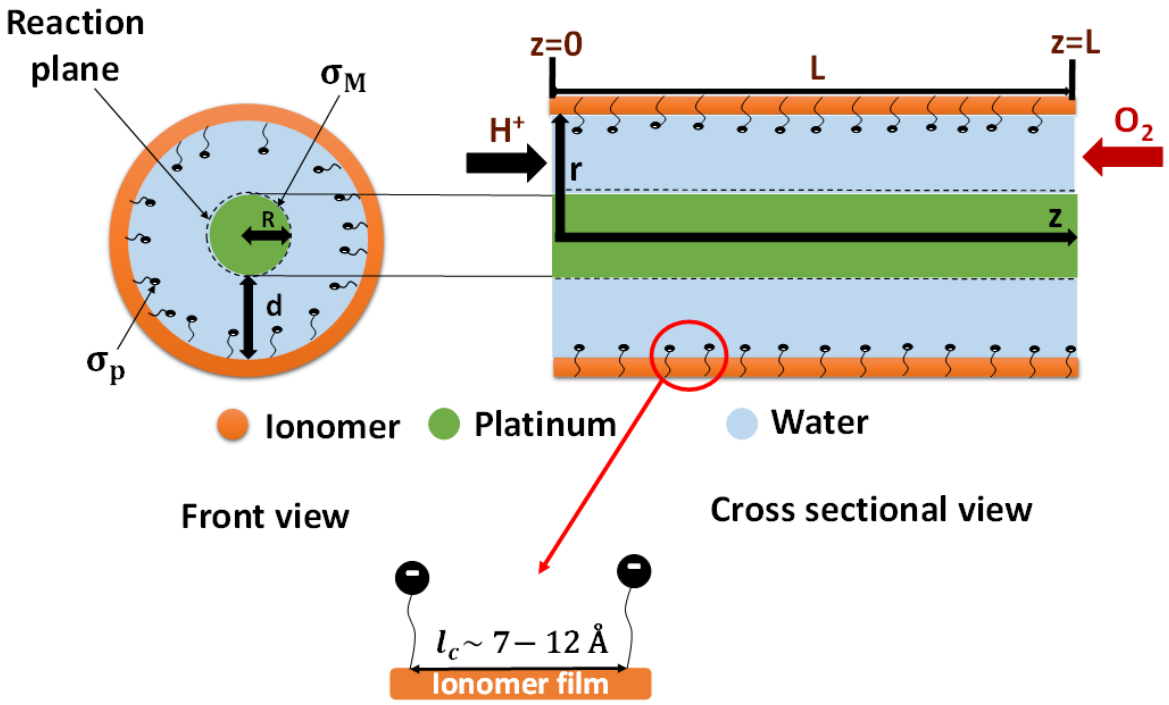
Reaction plane
σ_M
R
d
σ_p
z=0
L
z=L
H^+
r
z
O_2
Ionomer
Platinum
Water
Front view
Cross sectional view
$l_c \sim 7-12$ Å
Ionomer film

Figure 2

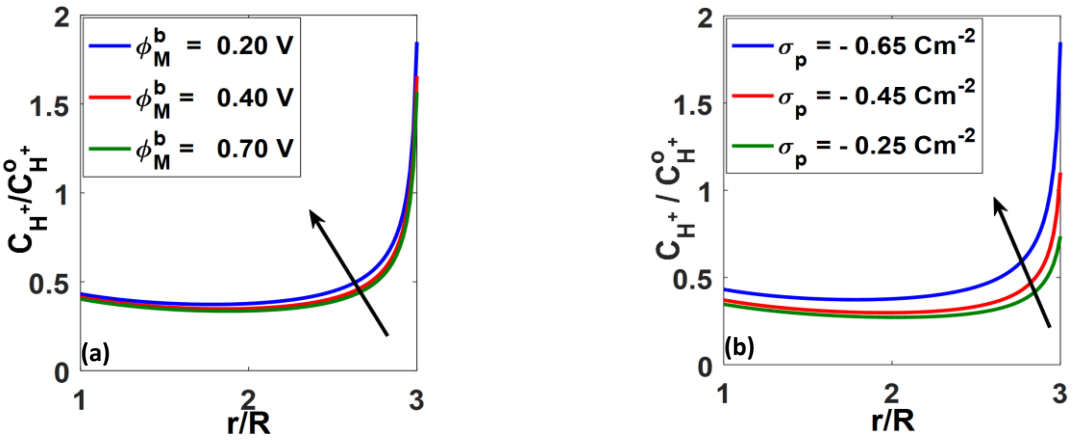
ϕ_M^b = 0.20 V
ϕ_M^b = 0.40 V
ϕ_M^b = 0.70 V
$C_{H^+}/C^o_{H^+}$
r/R
(a)
σ_p = - 0.65 Cm^{-2}
σ_p = - 0.45 Cm^{-2}
σ_p = - 0.25 Cm^{-2}
$C_{H^+}/C^o_{H^+}$
r/R
(b)

Figure 3

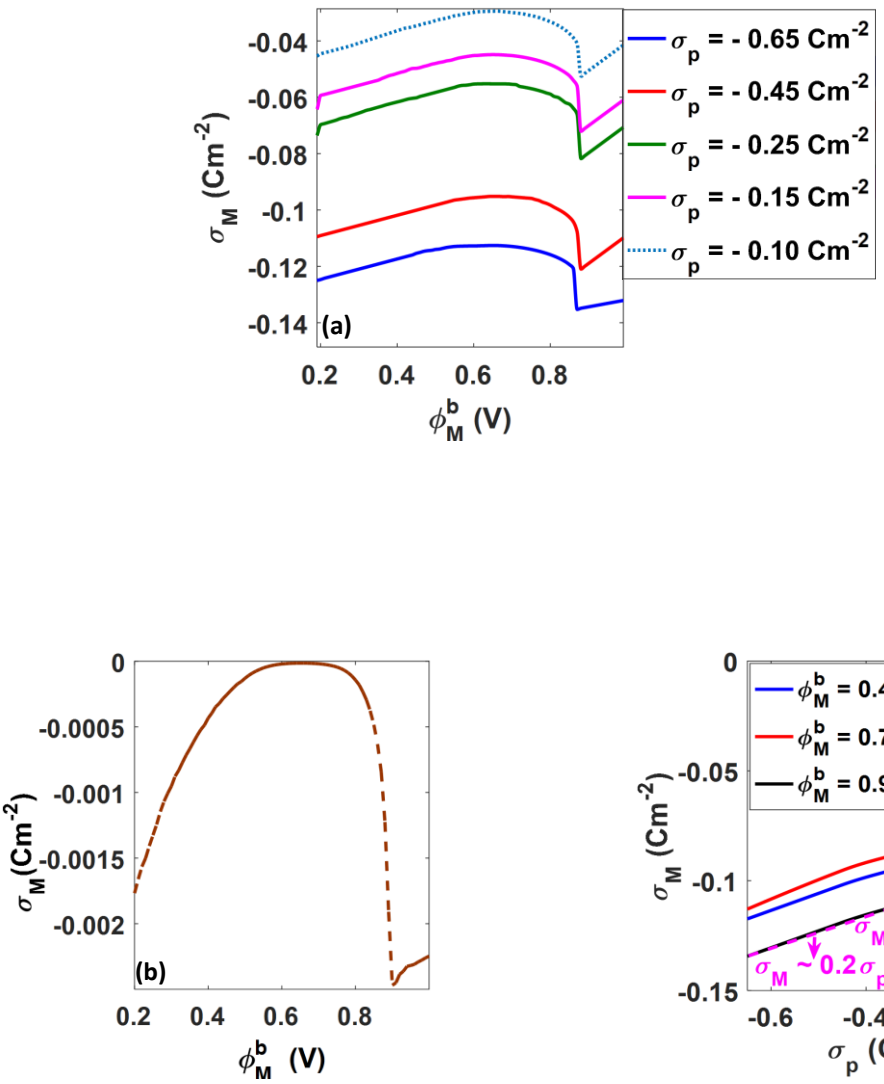
-0.04
-0.06
-0.08
-0.1
-0.12
-0.14
σ_M (Cm^{-2})
(a)
0.2
0.4
0.6
0.8
ϕ_M^b (V)
σ_p = - 0.65 Cm^{-2}
σ_p = - 0.45 Cm^{-2}
σ_p = - 0.25 Cm^{-2}
σ_p = - 0.15 Cm^{-2}
σ_p = - 0.10 Cm^{-2}
0
-0.0005
-0.001
-0.0015
-0.002
σ_M(Cm^{-2})
(b)
0.2
0.4
0.6
0.8
ϕ_M^b (V)
0
-0.05
-0.1
-0.15
σ_M (Cm^{-2})
ϕ_M^b = 0.4 V
ϕ_M^b = 0.7 V
ϕ_M^b = 0.9 V
σ_M ~ 0.5σ_p
σ_M ~ 0.2σ_p
(c)
-0.6
-0.4
-0.2
0
σ_p (Cm^{-2})
l_c ~ 10Å

Figure 4

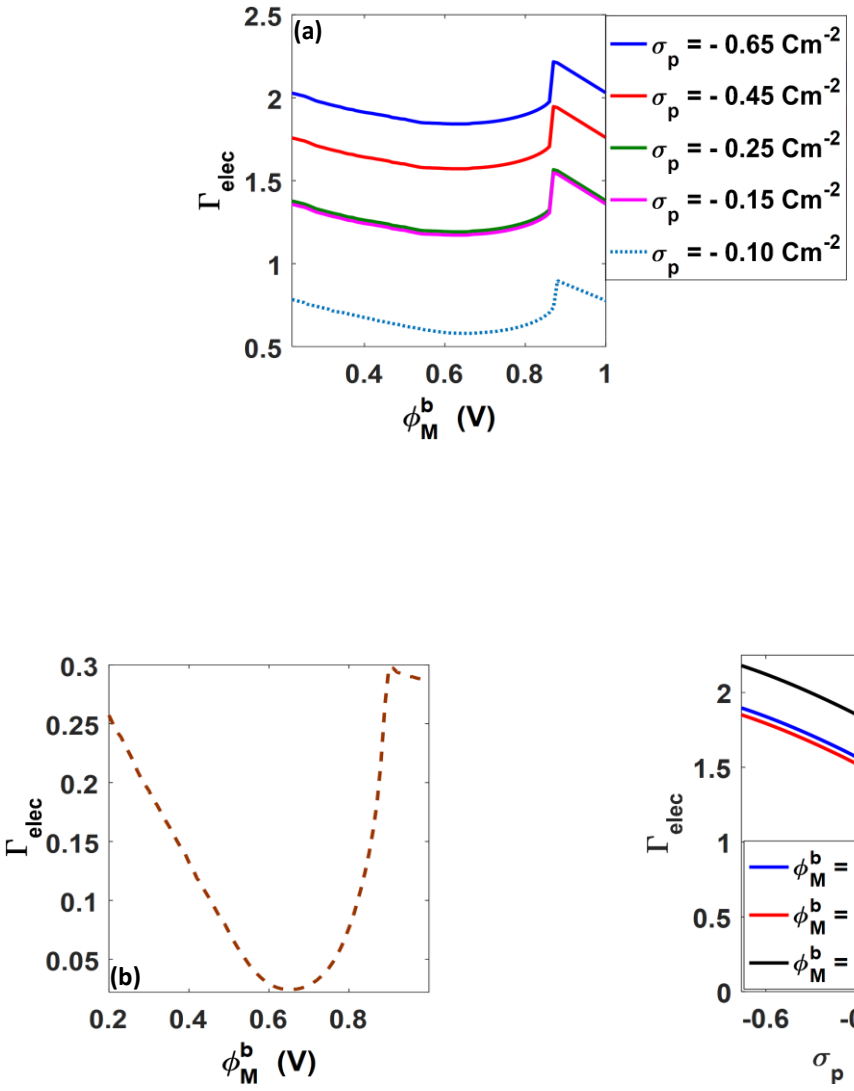
(a)
Γ_{elec}
ϕ_M^b (V)
σ_p = - 0.65 Cm^{-2}
σ_p = - 0.45 Cm^{-2}
σ_p = - 0.25 Cm^{-2}
σ_p = - 0.15 Cm^{-2}
σ_p = - 0.10 Cm^{-2}
(b)
Γ_{elec}
ϕ_M^b (V)
(c)
Γ_{elec}
ϕ_M^b = 0.4 V
ϕ_M^b = 0.7 V
ϕ_M^b = 0.9 V
σ_p (Cm^{-2})
l_c ~ 10 Å

Figure 5

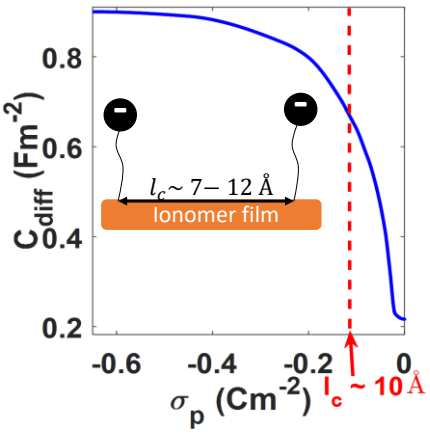
0.8
0.6
0.4
0.2
C_{diff} (Fm^{-2})
l_c~ 7– 12 Å
Ionomer film
-0.6
-0.4
-0.2
0
σ_p (Cm^{-2})
l_c ~ 10 Å

Figure 6

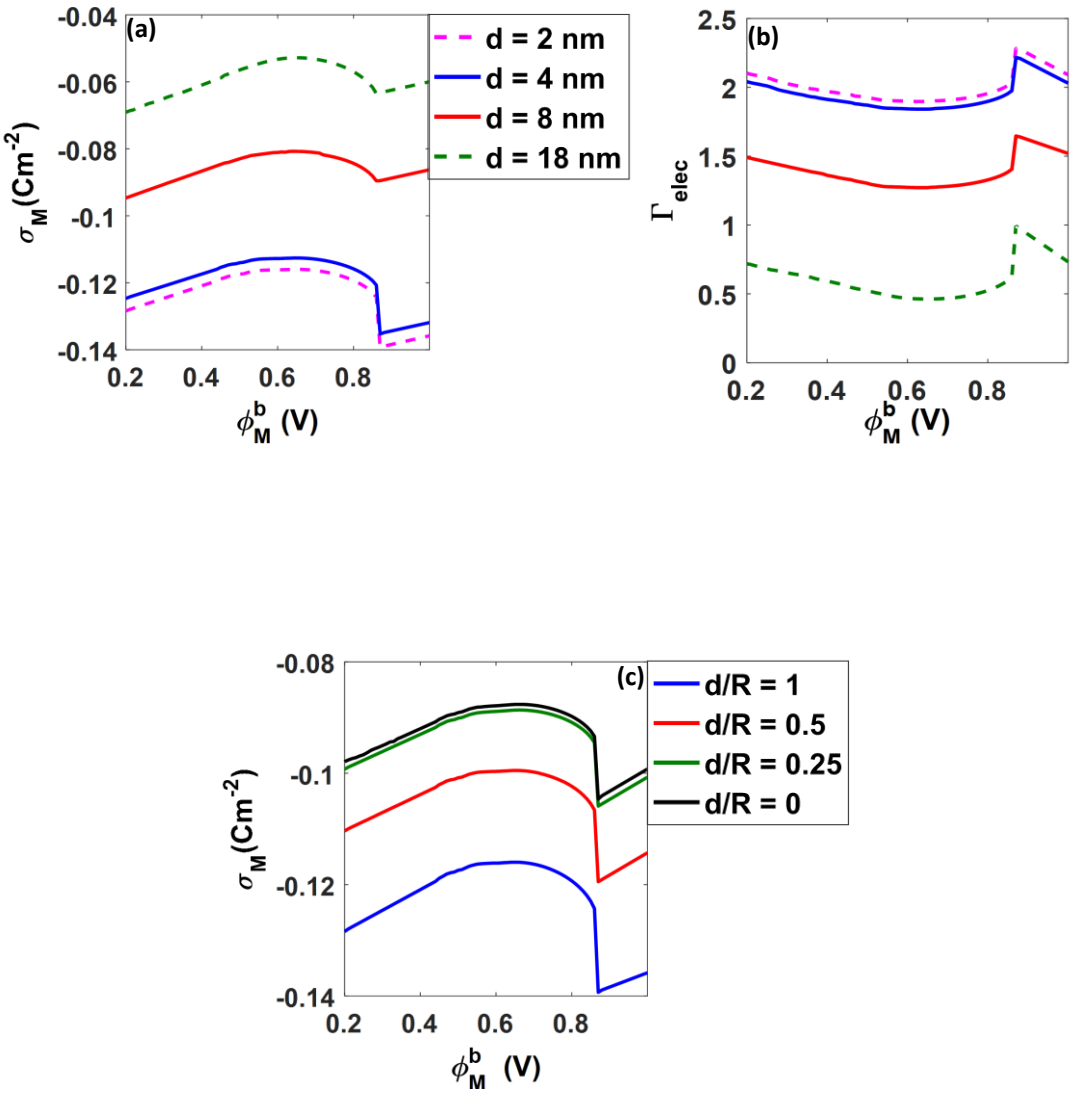
(a)
d = 2 nm
d = 4 nm
d = 8 nm
d = 18 nm
σ_M(Cm^{-2})
ϕ_M^b (V)
(b)
Γ_{elec}
ϕ_M^b (V)
(c)
d/R = 1
d/R = 0.5
d/R = 0.25
d/R = 0
σ_M(Cm^{-2})
ϕ_M^b (V)

Figure 7

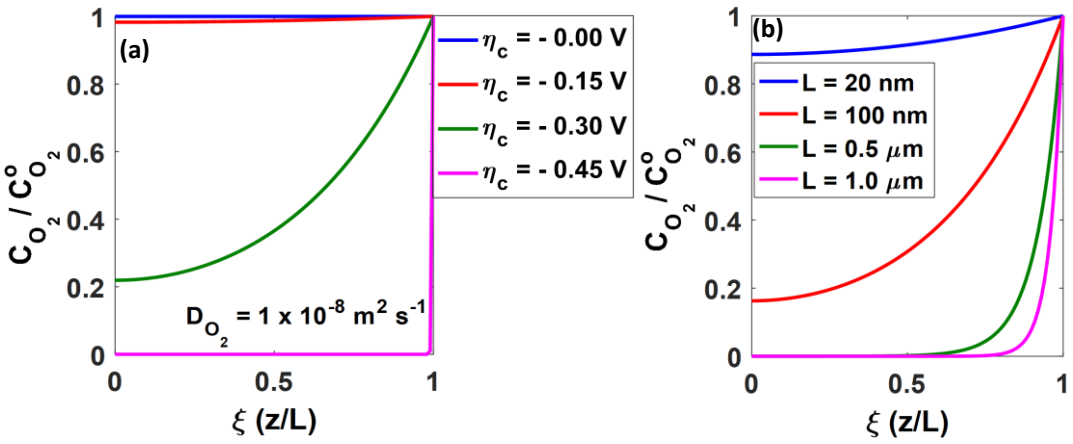
(a)
η_c = - 0.00 V
η_c = - 0.15 V
η_c = - 0.30 V
η_c = - 0.45 V
D_{O_2} = 1 x 10^{-8} m^2 s^{-1}
$C_{O_2} / C^o_{O_2}$
ξ (z/L)
(b)
L = 20 nm
L = 100 nm
L = 0.5 μm
L = 1.0 μm
$C_{O_2} / C^o_{O_2}$
ξ (z/L)

Figure 8

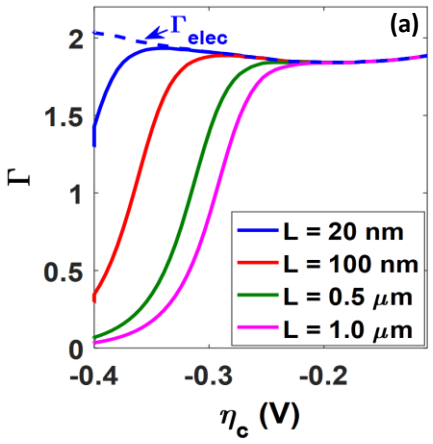
(a)
Γ_{elec}
2
1.5
1
0.5
0
Γ
-0.4
-0.3
-0.2
η_c (V)
L = 20 nm
L = 100 nm
L = 0.5 μm
L = 1.0 μm

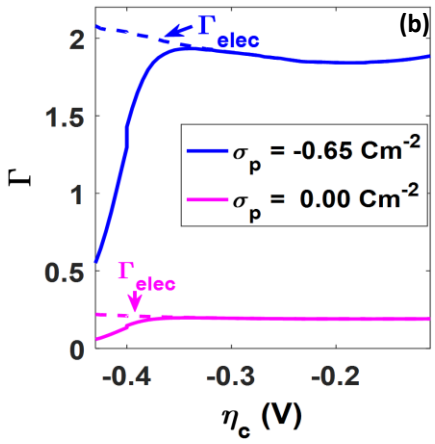
(b)
Γ_{elec}
2
1.5
1
0.5
0
Γ
-0.4
-0.3
-0.2
η_c (V)
σ_p = -0.65 Cm^{-2}
σ_p = 0.00 Cm^{-2}
Γ_{elec}

Figure 9

Table 1

Parameters		Values
ϕ^{pzc}	Potential of zero charge	0.3 V_{SHE} [24 –26]
γ_{O_2}	Reaction order of the ORR	1 [55–57]
γ_{H^+}	Reaction order of the ORR	1.5 – 1 [58]
α_c	Symmetry coefficient	0.5 – 1 [58]
T	Temperature	353 K
P	Pressure	1 atm
D_{O_2}	Oxygen diffusivity through water filled pore	1.0×10^{-4} cm^2s^{-1} [61]
D_{H^+}	Proton diffusivity through water filled pore	1.8×10^{-4} cm^2s^{-1} [65]
F	Faraday constant	96500 C mol^{-1}
l_c	Anionic surface groups separation	0.7 to 1.2 nm
H_{O_2}	Henry constant	5.9×10^{-4} mol $kg^{-1}bar^{-1}$ [62]
R_g	Gas constant	8.314 J $mol^{-1}K^{-1}$
ϵ	Dielectric constant	61 ϵ_O[62]
$C^o_{H^+}$	Reference proton concentration	1.25 M [63]
$C^o_{O_2}$	Reference oxygen concentration	3.2×10^{-4} M
σ_p	Ionomer surface charge density	-0.65 to 0.00 C m^{-2}
K_H	Helmholtz capacitance	0.2 F m^{-1} [64]
j^o	Exchange current density (low cd region)	1.96×10^{-9} A cm^{-2} [65]
j^o	Exchange current density (high cd region)	1.40×10^{-10} A cm^{-2} [65]
ϵ_{PtO}	Permittivity of oxide layer	30 ϵ_O [66]
ϵ_{IHP}	Permittivity of IHP	0.6 ϵ_O [67]
ϵ_{OHP}	Permittivity of OHP	30 ϵ_O [67]
δ_{PtO}	Thickness of the oxide layer	0.2 nm [28, 29]
δ_{IHP}	Thickness of IHP	0.275 nm (water dipole diameter)
δ_{OHP}	Thickness of OHP	0.515 nm [28, 29]
μ_w	Water dipole moment	3.1 D [68]
$\Delta\phi_M$	$\phi^b_M - \phi^s_M$	0.3 V [69]
ψ_{Ox}	Lateral interaction parameter	$64.2(1-\theta_{Ox})$ [28]
ς	Fractional charge number	0.8 [28]
E^o_{Ox}	Equilibrium potential of Pt oxidation	0.716 V [28]
R	Radius of the metal core	2 nm
R_2	Radius of the ionomer shell	$\geq$ 6 nm
d	Radius of the water filled pore	$\geq$ 4 nm

References

[1] T. Yoshida, K. Kojima, Interface Mag. 24 (2015) 45–49.

[2] J.-H. Wee, Renew. Sustain. Energy Rev. 11 (2007) 1720–1738.

[3] G.H. Tzeng, C.W. Lin, S. Opricovic, Energy Policy 33 (2005) 1373–1383.

[4] L.Carrette, K.A. Friedrich, U. Stimming, Fuel Cells 1 (2001) 5–39.

[5] M. Mench, Fuel Cell Engines, John Wiley & Sons, Ch. 1–4 (2007) 1–189 New Jersey.

[6] F. Barbir, PEM Fuel Cells: Theory and Prractice, Elsevier, Ch. 1–4 (2013) 1–72 Amsterdam.

[7] M. Eikerling, A.A. Kornyshev, A.A. Kulikovsky, Encyclopedia of Electrochemistry, VCH-Wiley, Ch. 8.2 (2007) 447–543 Weinheim.

[8] M. Eikerling, A. Kulikovsky, Polymer Electrolyte Fuel Cells: Physical Principles of Materials and Operation, CRC Press, Ch 1–3 (2014) 1–261 NewYork.

[9] K. Malek, T. Mashio, M. Eikerling, Electrocatalysis 2 (2011) 141–157.

[10] M. Uchida, Y. Aoyama, N. Eda, A. Ohta, J. Electrochem. Soc. 142 (1995) 463–468.

[11] M. Uchida, Y. Aoyama, N. Eda, A. Ohta, J. Electrochem. Soc. 142 (1995) 4143–4149.

[12] S. Litster, G. McLean, J. Power Sources 130 (2004) 61–76.

[13] M. Eikerling, J. Electrochem. Soc. 153 (2006) E58–E70.

[14] K. Malek, M. Eikerling, Q. Wang, T. Navessin, Z. Liu, J. Phys. Chem. C. 111 (2007) 13627–13634

[15] T. Soboleva, X. Zhao, K. Malek, Z. Xie, T. Navessin, S. Holdcroft, ACS Appl. Mater. Interfaces 2 (2010) 375–384.

[16] M. Eikerling, A.A. Kornyshev, J. Electroanal. Chem. 453 (1998) 89–106.

[17] T. Soboleva, K. Malek, Z. Xie, T. Navessin, S. Holdcroft, ACS Appl. Mater. Interfaces. 3 (2011) 1827–1837.

[18] K. Chan, M. Eikerling, J. Electrochem. Soc. 158 (2011) B18–B28 .

[19] I. V. Zenyuk, S. Litster, Electrochim. Acta 146 (2014) 194–206.

[20] I. V.Zenyuk, S. Litster, ECS Trans. 58 (1) (2013) 27–35.

[21] V. Climent, N. García-Araez, E. Herrero, J.M. Feliu, Russ. J. Electrochem. 42 (2006) 1145–1160.

[22] R. Gómez, J. Feliu, A. Aldaz, M.J. Weaver, Surf. Sci. 410 (1998) 48–61.

[23] M.J. Weaver, Langmuir. 14 (1998) 3932–3936.

[24] G.A. Attard, A. Ahmadi, J. Electroanal. Chem. 389 (1995) 175–190.

[25] T. Iwasita, X. Xia, J. Electroanal. Chem. 411 (1996) 95–102.

[26] H. Ebert, R. Parsons, G. Ritzoulis, T. Vandernoot, J. Electroanal. Chem. 264 (1989) 181–193.

[27] A. Frumkin and O. Petrii, Electrochim. Acta 20 (1975) 347–359.

[28] J. Huang, A. Malek, J. Zhang, M. Eikerling, J. Phys. Chem. C. 25 (2016) 13587–13595.

[29] J.Huang, J. Zhang, M. Eikerling, Faraday Discuss. 193 (2016), 427-446.

[30] E. Sadeghi, A. Putz, M. Eikerling, J. Electrochem. Soc. 160 (2013) F1159–F1169.

[31] A. Nouri-Khorasani, K. Malek, A. Malek, T. Mashio, D.P. Wilkinson, M.H. Eikerling, Catal. Today. 262 (2016) 133–140.

[32] R.H. Austin, C. Tung, G. Lambert, D. Liao, Chem. Soc. Rev. 39 (2010) 1049–1059.

[33] L. Bocquet, E. Charlaix, Chem. Soc. Rev. 39 (2010) 1073–1095.

[34] W. Sparreboom, A. Van Den Berg, J.C.T. Eijkel, New J. Phys. 12 (2010) 1–23.

[35] I. Vlassiouk, S. Smimov, Z. Siwy, ACS Nano. 2 (2008) 1589–1602.

[36] L.-H. Yeh, S. Xue, S.W. Joo, S. Qian, J.-P. Hsu, J. Phys. Chem. C. 116 (2012) 4209–4216.

[37] N. Hu, Y. Ai, S. Qian, Sens. Actuators B., 161 (2012) 1150–1167.

[38] B. Kim, J. Heo, H.J. Kwon, S.J. Cho, J. Han, S.J. Kim, G. Lim, ACS Nano. 7 (2013) 740–747.

[39] Z.S. Siwy, S. Howorka, Chem. Soc. Rev. 39 (2009) 1115–1132.

[40] H. Zhang, X. Hou, L. Zeng, F. Yang, L. Li, D. Yan, Y. Tian, L. Jiang, J. Am. Chem. Soc. 135 (2013) 16102–16110.

[41] R.D. Coalson, M.G. Kurnikova, Biological Membrane Ion Channels, Springer, Ch. 13 (1998) 450–484 NewYork.

[42] M. Eikerling, A. Kornyshev, E. Spohr, in Fuel Cells: Advances in Polymer Science, Springer, (2008) 15–54 Heidelberg.

[43] W. Im, B. Roux, J. Mol. Biol. 322 (2002) 851–869.

[44] S.Y. Noskov, W. Im, B. Roux, Biophys. J. 87 (2004) 2299–309.

[45] B. Nadler, U. Hollerbach, R. Eisenberg, Phys. Rev. E. 68 (2003) 1–9.

[46] P. Graf, M.G. Kurnikova, R.D. Coalson, A. Nitzan, J. Phys. Chem. B. 108 (2004) 2006–2015.

[47] B. Corry, S. Kuyucak, S.-H. Chung, Biophys. J. 84 (2003) 3594–3606.

[48] P. Choi, N.H. Jalani, R. Datta, J. Electrochem. Soc. 152 (2005) E123–E130.

[49] R. Triolo, A.H. Narten, J. Chem. Phys. 63 (1975) 3624–3631.

[50] Y. Guissani, B. Guillot, S. Bratos, J. Chem. Phys. 88 (1988) 5850–5856.

[51] J. Lobaugh, G. a. Voth, J. Chem. Phys. 104 (1996) 2056–2069.

[52] M.E. Tuckerman, G.J. Martyna, J. Phys. Chem. B. 104 (2000) 159–178.

[53] Q.P. Wang, M. Eikerling, D.T. Song, Z.S. Liu, J. Electrochem. Soc. 154 (2007) F95–F101.

[54] P. Berg, K. Ladipo, Proc. R. Soc. A Math. Phys. Eng. Sci. 465 (2009) 2663–2679.

[55] S. Trasatti, in: Advances in Electrochemistry and Electrochemical Engineering, Interscience, Vol. 10 (1977) NewYork.

[56] F. Tian, R. Jinnouchi, A.B. Anderson, J. Phys. Chem. C. 113 (2009) 17484–17492.

[57] N. Garcia-Araez, V. Climent, J. Feliu, J. Phys. Chem. C. 113 (2009) 9290–9304.

[58] D. Sepa, M. Vojnovic, and A. Damjanovic, Electrochim. Acta 32 (1987) 129–134.

[59] D. Sepa, M. Vojnovic, and A. Damjanovic, Electrochim. Acta 26 (1981) 781–793.

[60] A. Parthasarathy, J. Electrochem. Soc. 139 (1992) 2856–2862.

[61] J.R. Welty, C.E. Wicks, R.E. Wilson, G.L. Rorrer, Fundamentals of Momentum, Heat, and Mass Transfer, Wiley, Ch. 16 (2008) 217–223 NewYork.

[62] "NIST Chemistry WebBook," NIST, [Online]. Available: http://webbook.nist.gov/chemistry/. [Accessed 16 March 2016].

[63] P.D. Beattie, F.P. Orfino, V.I. Basura, K. Zychowska, J. Ding, C. Chuy, J. Schmeisser, S. Holdcroft, J. Electroanal. Chem. 503 (2001) 45–56.

[64] K. Kreuer, Proton Conductors: Solids, Membranes, and Gels—Materials and Devices, Cambridge University Press, Ch. 26 (1992) 409–416 Cambridge.

[65] A. Parthasarathy, S. Srinivasan, A. J. Appleby, C.R. Martin, J. Electrochem. Soc. 139 (1992) 2530–2537.

[66] G. Jerkiewicz, G. Vatankhah, J. Lessard, M.P. Soriaga, Y.S. Park, Electrochim. Acta 49 (2004) 1451–1459.

[67] J. Bockris, M. Devanathan, K Müller, Proc. R. Soc. London Ser. A. 274 (1963) 55–79

[68] D.D. Kemp, M.S. Gordon, J. Phys. Chem. A. 112 (2008) 4885–4894.

[69] V. Climent, G.A. Attard, J.M. Feliu, J. Electroanal. Chem. 532 (2002) 67–74.

[70] A.Z. Weber, A. Kusoglu, J. Mater. Chem. A Mater. Energy Sustain. 2 (2014) 17207–17211.

[71] A. Kongkanand, M.F. Mathias, J. Phys. Chem. Lett. 7 (2016) 1127–1137.

[72] S. Khanchandani, S. Kundu, A. Patra, A.K. Ganguli, J. Phys. Chem. C. 116 (2012) 23653–23662.